Available online at www.sciencedirect.com

jmr&t
Journal of Materials Research and Technology

journal homepage: www.elsevier.com/locate/jmrt

Original Article

# Investigating the time- and space- dependent mechanical, physical and chemical properties of aged polyethylene gas pipes using nanoindentation tests

*Sixi Zha* [a], *Hui-qing Lan* [a,*], *Nan Lin* [b], *Yueming Liu* [a], *Tao Meng* [b]

[a] *Laboratory of Vehicle Advanced Manufacturing, Measuring and Control Technology (Ministry of Education), Beijing Jiaotong University, Beijing, China*

[b] *China Special Equipment Inspection and Research Institute (CSEI), Beijing, 100029, China*

ARTICLE INFO

*Article history:*
Received 28 January 2023
Accepted 1 April 2023
Available online 7 April 2023

*Keywords:*
Polyethylene pipes
Aging
Creep
Nanoindentation
Mechanical properties

ABSTRACT

Macroscopic tensile tests are conventionally used to obtain mechanical properties of aged polyethylene (PE) gas pipes, but cannot characterize the inhomogeneous aging behavior of the specimens caused by diffusion-limited oxidation (DLO). Nanoindentation test procedures have, therefore, been adopted to obtain time- and space-dependent mechanical properties of small-sized PE pipe samples, especially, creep properties directly from two types of the PE pipes in accelerated aging and natural conditions. The results indicate that the energy-based method to calculate the initial contact stiffness is not only suitable for cementitious materials and rocks, but also for PE materials. The combination of nanoindentation creep test and generalized Kelvin model can extract detailed parameters that are more representative of the differences in material deformation. The change of crystallinity with aging times probably leading to the difference of mechanical properties was revealed by physical and chemical properties obtained by the DSC and FITR technique. In addition, the correlation between nanoindentation results and structural information also indicates crystallinity plays a dominant role on mechanical performances of the PE pipe. This method using nanoindentation can significantly promote the accuracy of mechanical properties characterization and possess well fitness for PE pipes in accelerated aging conditions or in-service.



## 1. Introduction

Polyethylene (PE) pipe is one type of important pressure-retaining structure in lifeline engineering, its properties play a significant role on the safety issues related to natural gas or water transportation, human life and property. Though PE pipes have many advantages, the aging of materials exposed to various environment is inevitable, which over time leads to

* Corresponding author.
E-mail address: hqlan@bjtu.edu.cn (H.-q. Lan).

https://doi.org/10.1016/j.jmrt.2023.04.004

**Nomenclature**

| | |
|---|---|
| $S$ | Contact stiffness, N/m |
| $P$ | Indentation load, mN |
| $h$ | Instantaneous indenter displacement, nm |
| $dP$ | The differential of indentation load in the upper portion of the unloading data |
| $dh$ | The differential of displacement in the upper portion of the unloading data |
| $P_{max}$ | Maximum indentation load, mN |
| $h_{max}$ | Maximum displacement, nm |
| $\nu_E$ | Elastic energy ratio |
| $W_s$ | Absolute work, mN·nm |
| $W_e$ | Elastic recovery, mN·nm |
| $W_{ir}$ | Irreversible energy work, mN·nm |
| $h_c$ | Contact depth, nm |
| $h_s$ | Vertical surface deflection, nm |
| $h_f$ | Residual deforcement, nm |
| $\varepsilon$ | Geometric constant |
| $E_r$ | Reduced modulus, GPa |
| $A_c$ | Contact area, $nm^2$ |
| $E$ | Elastic modulus of the sample, MPa |
| $E_i$ | Elastic modulus of the indenter, MPa |
| $\nu$ | Poisson's ratio of the sample |
| $\nu_i$ | Poisson's ratio of the indenter |
| $H$ | Hardness |
| $\psi$ | Plasticity index |
| $X_c$ | Crystallinity |
| $\Delta H_m$ | Melting enthalpy of the sample, J/g |
| $\Delta H_m^0$ | Melting enthalpy of 100% PE crystal, J/g |
| $CI$ | Carbonyl index |
| $\dot{\varepsilon}$ | Strain rate, equals to $d\varepsilon/dt$, $s^{-1}$ |
| $\sigma$ | Applied stress, GPa |
| $n$ | Stress exponent of creep |
| $h_e$ | Elastic deformation, nm |
| $h_{ev}$ | Viscoelastic deformation, nm |
| $h_v$ | Viscous deformation, nm |
| $h_i$ | Indentation depth for ith Voigt element, nm |
| $t_i$ | Delay time for ith Voigt element, s |
| $\mu_0$ | Viscosity coefficient, s/nm |

a deterioration in mechanical, physical and chemical properties and a decrease in operational safety [1–3]. Over the past three decades, many studies have paid much attention to the degradation or deterioration of PE pipes under different conditions, e.g. chlorinated water, heated air or natural exposure [4–8]. Currently, artificial accelerated methods are generally used to shorten the aging time of PE pipes, for instance, the thermo-oxidative aging testing is one of them. In terms of PE gas pipe, they are generally exposed to oven and aged at the temperature under but close to the melting point of polyethylene [9]. Unfortunately, the assessment method based on the usage of accelerated testing seems to arise a new insoluble problem-the divergence between natural and accelerated aging behavior. For example, an unavoidable difficulty is the diffusion-limited oxidation (DLO) behavior caused by accelerated testing. Actually, the purpose of accelerated testing is to obtain similar aging and degradation results in a short period of time as after a long-term operation. Therefore, an in-depth study of the aging mechanism is needed. In terms of the inhomogeneous aging caused by DLO, it is generally believed to occur in high temperature environments, but a report indicates that significant non-uniform aging behavior also occurs under two years of continuous solar exposure [8]. The nature of this mechanism causes the aging of the material to be concentrated on the surface, while the interior remains relatively resistant [10–13]. The higher the temperature is, the more obvious the DLO phenomenon becomes and the surface material deteriorates.

There is still a lack of standardized method to assess the safety of PE gas pipes, so it is of great importance to evaluate the technical properties of PE gas pipe and decide whether to replace it or not. Research shows that the most commonly used tensile test for obtaining the mechanical properties of PE pipes contains information on potential material defects [7,14], and therefore cannot reveal the time- and space-dependent mechanical properties under accelerated or natural conditions, especially, inhomogeneous aging behavior of the specimens caused by DLO. In addition, the key performance parameters obtained by differential scanning calorimeter (DSC), Infrared spectroscopy (IR) or Raman spectroscopy based testing methods do not characterize the mechanical behavior of the material. Further, there is a lack of established link between the physical, chemical properties of polyethylene pipe and the mechanical properties of the material. Therefore, there is an urgent need for a microscale mechanical testing method that mirrors the inhomogeneous degradation process of the material and has a good connection and interpretation with the physical or chemical properties.

Researchers are all the way seeking reliable, faster and easier durability testing methods, small sample testing or nondestructive detection, to enable in-service pipeline aging assessment. However, in reality, this ideal assessment would be difficult to achieve, because the conventional testing techniques would face great challenge when applied to PE materials which is susceptible to photo-oxidative and thermo-oxidative aging, and the PE pipe, as a structure, would include remarkable effects of slow crack growth and residual stresses, etc. Over the past two decades, nanoindentation technique had been commonly used to characterize the micro-mechanical behavior of materials [15,16]. Due to its good accuracy, it is widely used to characterize the local mechanical properties of materials and thus the inhomogeneous properties of materials [17,18]. Relative researches came from various institutions with a very diverse range of themes, including rocks [19], polymers [20–23], polymer-based composites [24,25], coatings [26] and films [27–29], etc. These researches paid much attention to the mechanical properties of the materials, as well as the influence of other factors on these properties, such as changes in indentation creep properties caused by increasing environmental temperature or operational time [30]. Moreover, nanoindentation can be used to obtain parameters such as the local elastic modulus and hardness of the material, which can be linked to other parameters such as crystallinity and fracture toughness of the material. Thus, it is possible to clearly characterize the

material properties and explain their intrinsic mechanisms [31]. Furthermore, nanoindentation can be used to detect and study the early changes in mechanical properties of polymer caused by aging, as long as macro-structural factors (such as cracks) do not exist [32]. There are few studies on the correlation between nanoindentation results and structural information that can be extracted by other methods. The parameters of local micro-mechanical properties suffering from different aging conditions will be of great importance to support the failure analysis of PE pipes as well as the accurate lifetime prediction.

In this paper, we simulated the operating conditions of pressured gas pipelines and conducted artificial accelerated aging tests on PE pipes using a unique aging device-thermo-oxidative aging system. Then, DSC, ATR-FTIR and nanoindentation creep tests were used to characterize the non-uniform aging behavior of PE gas pipe by thermo-oxidative aging. The mass crystallinity was obtained from the melt enthalpy calculation of the DSC curve. The indentation curves were used to obtain the elastic modulus, hardness, creep depth and plasticity index of the PE samples, and then the correlation between its aging degradation and micro-mechanical behavior, i.e., the relationship between crystallinity and elastic modulus, was demonstrated. Moreover, the generalized Kelvin model was used to fit the time-dependent the parameters related to the creep parameters of polyethylene.

## 2. Materials and methods

### 2.1. Materials and aging procedure

Two commonly used PE gas pipe, made of unimodal PE80 resin and bimodal PE100 resin, were supplied by Nam Sok Building Material & Plastic Products (Shenzhen) Co, Ltd, where the ratio of pipe diameter to wall thickness, i.e. the standard dimension ratio (SDR) is 11. Thermo-oxidative process was carried out on a unique aging device which provide the high temperature and high internal pressure environment for sealed PE pipes with end caps. The basic structure of the apparatus is briefly shown in Fig. 1, and the real photo of this device has been exhibit in our another work [7]. To control the internal pressure of PE pipes, an arithmetic program was compiled to control the sensor and the solenoid valve. Two manual ball valves are used to release and restore the air pressure inside pipes when the specimen is replaced. The relief valve is used to prevent abnormal pressure rise inside pipes due to program error or operational error. Exposure times were determined for the purpose of observing significant aging behavior as far as possible and based on preliminary tests. Comparing to natural gas, air was chosen as the medium for safety consideration, where the pressure was set as 0.4 MPa and the temperature was set as 80 °C. A series of PE pipe samples were removed on specific times (0 h, 672 h, 1344 h, 2352 h, 3024 h and 10104 h for PE80 and 0 h, 672 h, 1344 h, 2016h, 2688 h and 10104 h for PE100) and cooled immediately to room temperature in preparation for characterization tests. In addition, two types of PE pipes buried in soil with the service life (15 years of PE100 and 25 years of PE80) was obtained from Shenzhen Gas Group Co, Ltd.

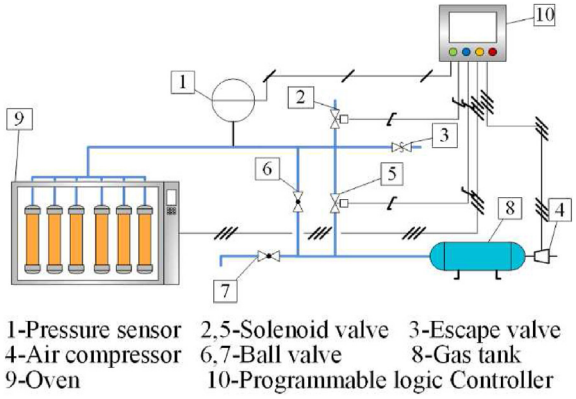


**Fig. 1 – Schematic diagram of thermo-oxidative aging system.**

### 2.2. Nanoindentation

Nanoindentation testing was conducted at room temperature of 23 (±2)°C on PB1000 (NANOVEA, USA). The general arrangement of instrument components and samples are shown schematically in Fig. 2, including optics system, nanoindentation probe, samples and insulation block. One set of nanoindentation experimental schemes was designed: the target load is set as 1000 μN, loading and unloading rate remained at 2000 μN/min. Typical creep curves of the nanoindentation test (peak loading equals to 1000 μN and holds 30s) would be obtained. The pipe was taken out at each stated aging time and a 5 mm thick fan-shaped piece was cut out along the radial direction of the pipe.

The specific sample making process was roughly carried out following the three steps shown in Fig. 3. In the first step, the PE pipes with different aging times were taken out from the oven and cut into rings with a thickness of 5 mm, where the rings were thick enough to eliminate the influence of the substrate (generally, maximum indentation depth at the peak load <10% of the sample thickness) [33] and the axial residual stress can be ignored according to the related perspective at the same time [34]. In the second step, small samples were cut from the ring to facilitate pasting on the standard metal block. In the third step, the specimens were fixed to the metal block

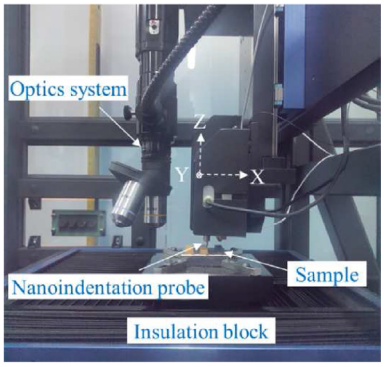


**Fig. 2 – Schematic representation of the experimental configuration for nanoindentation.**

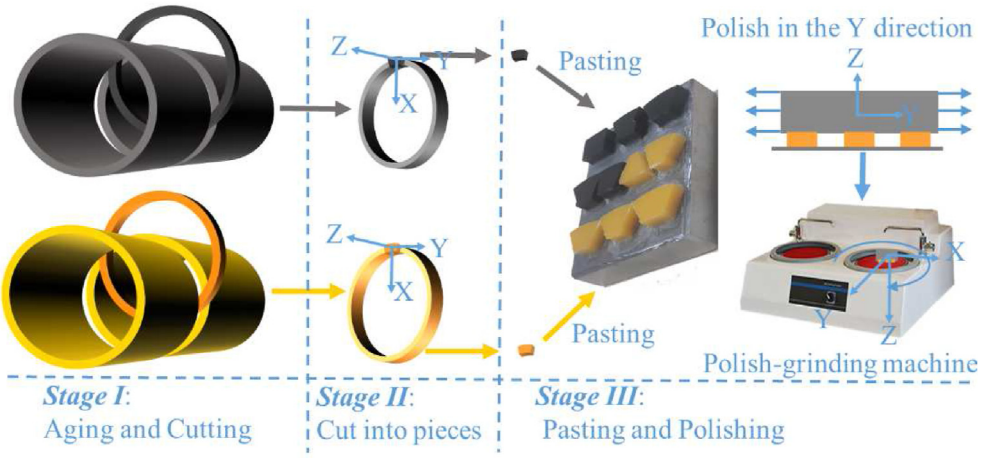


**Fig. 3 – Preparation of testing specimens for nanoindentation testing.**

in the order of different aging times. Since the surface roughness during nanoindentation directly affects the determination of the effective zero point of contact as well as the indentation displacement measurement, the PE pipe must be polished. The polishing needs to be done along the Y-direction to avoid rounding of the radial (X-direction) boundary of the pipe to be measured. In this paper, the polish-grinding machine was used for grinding and then polishing until the surface roughness did not have a significant effect on the results [35]. The surface roughness of the nanoindentation specimen was around 10 nm, and the ratio of roughness or depth deviation to indentation depth (the minimum indentation depth is about 200 nm in this paper) was less than 0.05, which can guarantee hardness deviation within 10% [36,37].

The output data of the nanoindentation experiment was analyzed according to the most common methods developed by Oliver and Pharr [35] to calculate the mechanical properties of the material. Fig. 4 shows the typical indentation curve which consists of three stages of loading, holding and unloading, where the different line type blocks represent different works [19,24]. In the loading stage, the applied load increases with the increment of indentation depth. This stage can be regarded as the combination of elastic and plastic deformation, whereas during the unloading stage we can assume that only elastic deformation can be recovered, and this is used to calculate the mechanical properties. Fig. 5 illustrates the unloading process during a typical nanoindentation test. The blue dash line in Fig. 5 represents the boundary of the indenter and the yellow solid line represents the upper surface of the specimen [35]. Under the external load P, the indenter was pressed into the surface of the specimen to be tested. After reaching the maximum depth, unloading was performed and residual deformation was left behind. The symbols of the various parameters listed in Fig. 5 were used to calculate the characteristic parameters such as elastic modulus, hardness and plasticity index of the specimen.

In order to estimate elastic modulus and hardness values, several parameters derived from Figs. 4 and 5 were analyzed. Especially, the calculation of contact stiffness was used two methods in this paper. In the classical Oliver and Pharr method (O–P method), initial contact stiffness S defined as the slope of the upper portion of the unloading part (70%~90% of $h_{max}$), as shown in Fig. 4, can provide us with valuable information regarding the mechanical response of the material. However, due to the viscosity of the PE pipe, its maximum indentation depth occurs in the unloading stage (called nose phenomenon [38]), which might make it impossible to calculate the initial contact stiffness using the slope. Therefore, indentation tests were performed with holding loads for 30s to eliminate the imprecision in determinant of the slope. In addition, material response during the nanoindentation holding stage can also be used to model creep properties. Moreover, in order to compare with O–P mehtod, the energy-based analysis suitable for cementitious materials or rocks was also used to calculate the initial contact stiffness in this paper, and the latter method can eliminate the influence of the indenter bluntness on the test results [19,39]. It should be

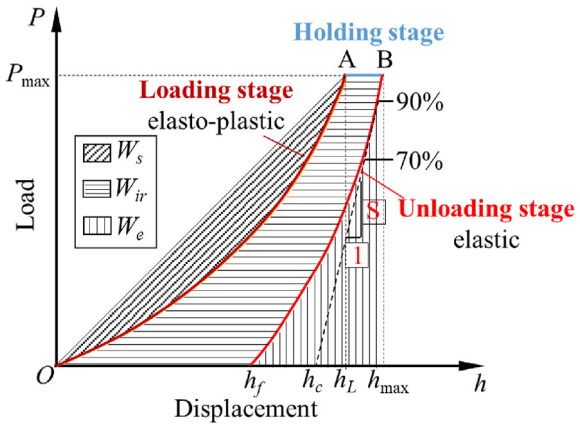


**Fig. 4 – Schematic illustration of indentation load–displacement curve and the energy analysis for calculation purposes.**

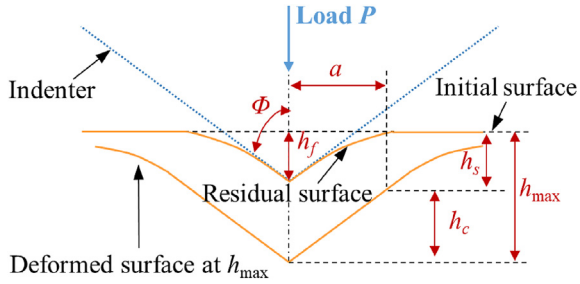


**Fig. 5 – Illustration loading-unloading process of indentation testing.**

noted that the two methods only differ in the calculation of contact stiffness, while all other parameters are calculated in the same way.

$$\begin{aligned} &\text{O}-\text{P method}: S=\frac{dP}{dh} \\ &\text{Energy}-\text{based method}: S=0.75\times(2\nu_E-1)\frac{P_{max}}{h_{max}} \end{aligned} \tag{1}$$

where $\nu_E$ is the elastic energy ratios which can be defined as the ratio of the absolute work and the elastic work (in Fig. 4):

$$\nu_E=\frac{W_s}{W_e} \tag{2}$$

where $W_s$ is the absolute work from nanoindentation determined by the area $OAh_LO$, and $W_e$ is the elastic recovery calculated by the area $h_fBh_{max}h_f$.

$$h_{max}=h_s+h_c \tag{3}$$

$$h_s=\varepsilon\frac{P_{max}}{S},\ \varepsilon=0.75 \tag{4}$$

$$h_c=h_{max}-0.75\times\frac{P_{max}}{S} \tag{5}$$

where $h_s$ is the vertical surface deflection at the perimeter of the contact and $h_c$ is the contact depth.

Once initial contact stiffness and contact depth were derived, the reduced elastic modulus and contact area can be calculated as [40] :

$$E_r=\frac{\sqrt{\pi}S}{2\sqrt{A_c}} \tag{6}$$

$$A_c=24.5h_c^2 \tag{7}$$

Finally, the elastic modulus and hardness can be obtained as:

$$\frac{1}{E_r}=\frac{1-\nu^2}{E}+\frac{1-\nu_i^2}{E_i} \tag{8}$$

$$H=\frac{P_{max}}{A_c} \tag{9}$$

where $E$ and $E_i$ are the elastic modulus of the sample and the indenter, respectively, $\nu$ and $\nu_i$ are the Poisson's ratio. To calculate elastic modulus of the samples to be measured, Eq. (8) is transformed to:

$$E=\frac{1-\nu^2}{\frac{1-\nu_i^2}{E_i}+\frac{1}{E_r}} \tag{10}$$

where $E_i$ equals to 1140 GPa and $\nu_i$ equals to 0.07 [20], and Poisson's ratio of PE is regarded as 0.45. What's more, it is considered that the Poisson's ratio of PE remains constant during aging.

Plasticity of the material is expressed as the permanent deformation under loads. The areas under the load–displacement curve during loading and unloading can be used to quantify the plasticity of the material. In this paper, a parameter 'plasticity index' was used to characterizes the relative plastic/elastic behavior of the material when it undergoes external stresses and strains. In the case of indentation contacts, one of the possible definitions for the plasticity index might be obtained from the compliance method tests, where the index may be as follows [40,41]:

$$\psi=\frac{W_{ir}}{W_{ir}+W_e} \tag{11}$$

where $W_{ir}$ is the irreversible energy work determined from the area $OABh_f$ in Fig. 4.

According to this definition, $\psi=0$ for fully elastic cases and $\psi=1$ for a fully plastic deformation. For other materials, $0<\psi<1$.

As mentioned before, nanoindentation technique has been widely used to assess the creep behavior of materials [42,43]. Generally, there are three stages in a macroscale creep test: transient (stage I), quasi-steady (stage II), and accelerating (stage III). Most nanoindentation cases show only the first two stages because the materials would not rupture owing to the local load [44]. The Stage I is the transient creep stage where the creep displacement with an initial rapid increase is progressively slowed down due to the occurrence of creep resistance or strain hardening. After the transient stage, the creep displacement turns to increase at a nearly constant rate, which hints the appearance of Stage II, namely the quasi-steady creep stage. The relationship between creep rate and the stress exponent is based on the following power–law relation [45,46].

$$\dot{\varepsilon}\sim\sigma^n \tag{12}$$

Where $\dot{\varepsilon}$ is the strain rate, $\sigma$ is the applied stress and $n$ is the stress exponent of creep which is determined through anteriorly identifying the equivalent values of stress and strain rate in the quasi-steady creep stage. The equivalent strain rate and stress obey the following scaling relations.

$$\dot{\varepsilon}\sim\frac{1}{h}\frac{dh}{dt},\sigma\sim\frac{P}{h^2} \tag{13}$$

The mechanical responses of the polymer can be described by the theoretical model consists of springs and dashpots. In this paper, the generalized Kelvin model model was suggested to describe the indentation creep displacement responses of PE materials during the holding stage. Based on this model, the total displacement of two PE materials during the holding stage $h(t)$ can be fitted by using the following equation [47].

$$h(t) = h_e + h_{ev} + h_v \tag{14}$$

$$h_{ev} = \sum_{i=1}^{3} h_i\left(1 - e^{-t/t_i}\right), h_v = t / \mu_0 \tag{15}$$

Where $h_e$, $h_{ev}$ and $h_v$ are elastic, viscoelastic and viscous deformation. It should be pointed out that $h_{ev}$ in this paper is described by three Voigt elements. $h_i$ and $t_i$ are the indentation depth and delay time for ith Voigt element. $\mu_0$ is the viscosity coefficient of the single dashpot in the generalized Kelvin model.

### 2.3. *Differential Scanning Calorimetry*

Thermal analysis was carried out by Differential Scanning Calorimetry (DSC) of the type DSC 200F3 (NETZSCH Group, Germany). The samples were continuously heated up from room temperature to 300 °C with a heating rate of 20 °C/min. In terms of polymer samples, the effect of their heat treatment or heating history on the polymer properties can be studied with the results of a single heat-up process, and the crystallinity can be calculated. Approximate 1 mm thick material of the inner surface, middle layer and outer surface of the aged PE pipe were removed for testing according to different aging times. The output data of the DSC experiment was analyzed according to the most common methods to calculate the physical properties of the material. For instance, the crystallinity ($X_c$) was calculated from the melting enthalpy of the DSC curve by the following formula:

$$X_c = \frac{\Delta H_m}{\Delta H_m^0} \tag{16}$$

where $\Delta H_m$ is the melting enthalpy of the tested sample, and $\Delta H_m^0$ is the melting enthalpy of 100% PE crystal, which equals to 293J/g [48].

### 2.4. *Infrared spectroscopy*

IR spectra were collected with an ATR-FTIR spectrometer, using a 4 $cm^{-1}$ spectral resolution and 30 scans per specimen. To characterize potential changes in the chemical structure during the exposure time, ATR- FTIR spectroscopy measurements were completed with a device of the type Bruker VERTEX 70 (Bruker Corporation, Germany). The ATR-FTIR for ranges from 400 to 4000 $cm^{-1}$ was used to analyze the variation in functional groups of pipe samples due to exposure to heater air. The aging degree is characterized by the carbonyl index (CI), which was calculated from the ratio between the integrated band absorbance of the carbonyl peak from 1650 to 1850 $cm^{-1}$ and that of the methylene ($CH_2$) scissoring peak from 1420 to 1500 $cm^{-1}$ as expressed in the following equation [49]:

$$CI = \frac{\text{Area under band } 1650 - 1850\ cm^{-1}}{\text{Area under band } 1420 - 1500\ cm^{-1}} \tag{17}$$

## 3. Results and discussions

### 3.1. *Nanoindentation testing results*

Fig. 6 exhibits typical load–displacement curves of the outer layer of PE80 and PE100 pipe samples at the different aging times, respectively. The maximum indentation depths (the displacement in the indenting direction) decreased with the exposure time for both samples, and the indentation depth of PE100 were smaller than PE80 samples at early stage of accelerated test, implying the PE100 material is stiffer than the PE80 material. However, it is worth noting that the indentation depth of the PE80 pipe samples is smaller than the PE100 with further exposure in oven, which implies the PE80 pipe might be more affected by thermo-oxidative aging. In addition, the two curves at the leftmost end in Fig. 6 (a) and (b) show that the aging degree of PE80 pipe after exposing to heated and pressured air about 10104 h is comparable to the result of 25 years of service, and PE100 after 10104 h exposure is close to the result of PE100 pipe servicing for 15 years. As

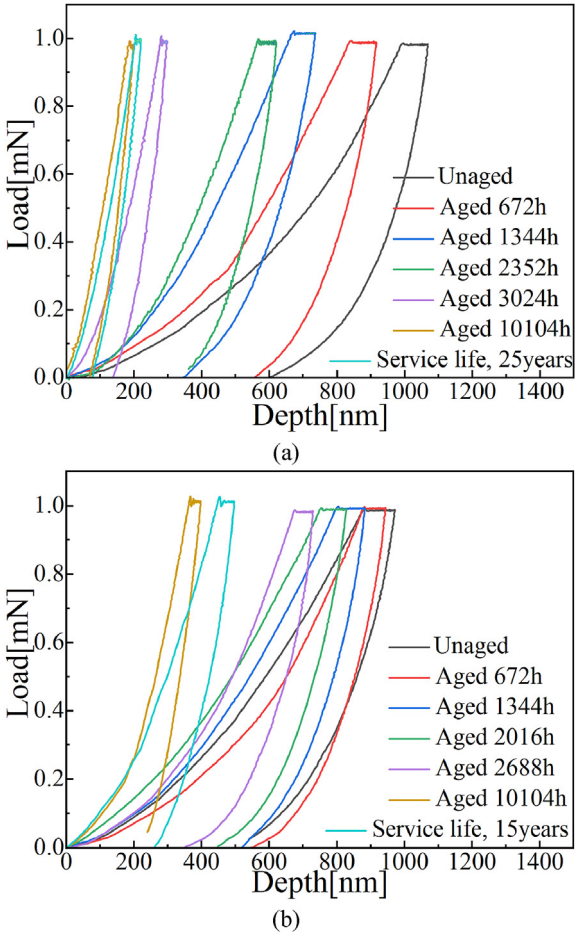


**Fig. 6 – Typical load–displacement curves in outer layer of PE80 pipe (a) and PE100 (b) samples with different aging times.**

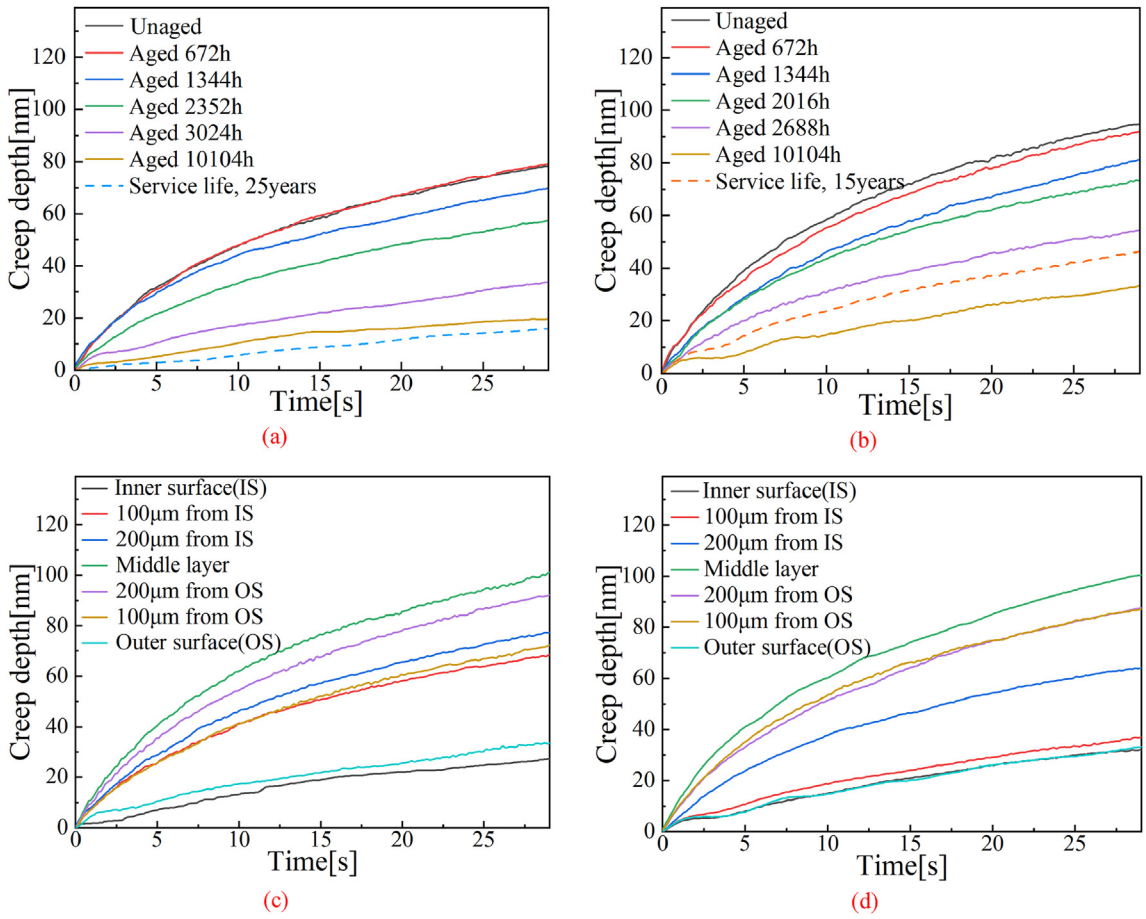


**Fig. 7 – The creep depth curves on the outer surface with different exposure times for PE80 (a), and PE100 (b), with different positions of PE80 after aged 3024 h (c), and PE100 after aged 10104 h.**

mentioned in Fig. 4, the curves could be divided into three stages, where the horizontal segment represents the holding stage and reveals the creep process. It can also be crudely observed from Fig. 6 that the creep depth is positively correlated with the maximum indentation depth i.e., both the maximum indentation depth and the creep depth decrease with the aging times. In the following pages, the corresponding values of creep depths or maximum indentation depths will be extracted for further analysis.

Fig. 7(a) and (b) present the creep behaviors of the two types of the PE pipes at different aging times. In these tests, the loading of 1 mN was held for 30s. In regard to all specimens, the creep deformation decreased with exposure times. At each aging time, the creep depth of the PE100 pipe specimens is almost greater than that of the PE80 pipe specimens, which elucidated PE80 specimens show higher resistance to creep. The above difference between the two materials in the creep resistance (creep and relaxation are essentially the same) might be due to the higher molecular mobility of PE100 than PE80 [50]. Compared to PE100, the chains in PE80 with lower-density entanglements become oriented more easily which, in turn, reduces molecular mobility and leads to lower relaxation time or creep depth [51]. Similarly, the creep curve of the PE80 after aged 10104 h was closer to the results of the PE80 pipe servicing for 25 years, while the creep depth of the PE100 after aged 10104 h was smaller than the result of PE100 pipe servicing for 15 years. Fig. 7 (c) and (d) show the creep curves at different positions on the samples after aged 3024 h for PE80 and 10104 h for PE100, respectively. It can be seen that the creep depth of the middle layer was greater than that of the inner and outer layers of the pipe, which indicates the non-middle layer shows higher resistance to creep after a long term of exposure in high temperature and pressure.

Fig. 8(a) and (b) exhibit the creep depth and the maximum indentation depth of PE80 and PE100 pipe specimens at different exposure times and different positions, respectively. In particular, Fig. 8(a) gives the specific values of creep depth vs aging time for the curves in Fig. 7(a) and (b), and Fig. 8(b) gives the specific values of creep depth vs spatial location for the curves in Fig. 7(c) and (d), as well as the specific values of maximum indentation depth vs spatial location. The results demonstrate that the creep depth of the specimens shows an obvious characteristics of the space-time distribution with the increment of aging times. As shown in Fig. 8(a), it can be seen that the stepwise increments in exposure time to the heated and pressured air induces a significant reduction in the creep depth of the outer layer of the pipe but a slow decrease of the middle layer. In detail, the data show that the creep depth of middle layer of the PE80 and PE100 specimen decreases by 9.1% and 20.5% respectively, while it decreases by 75.6% and

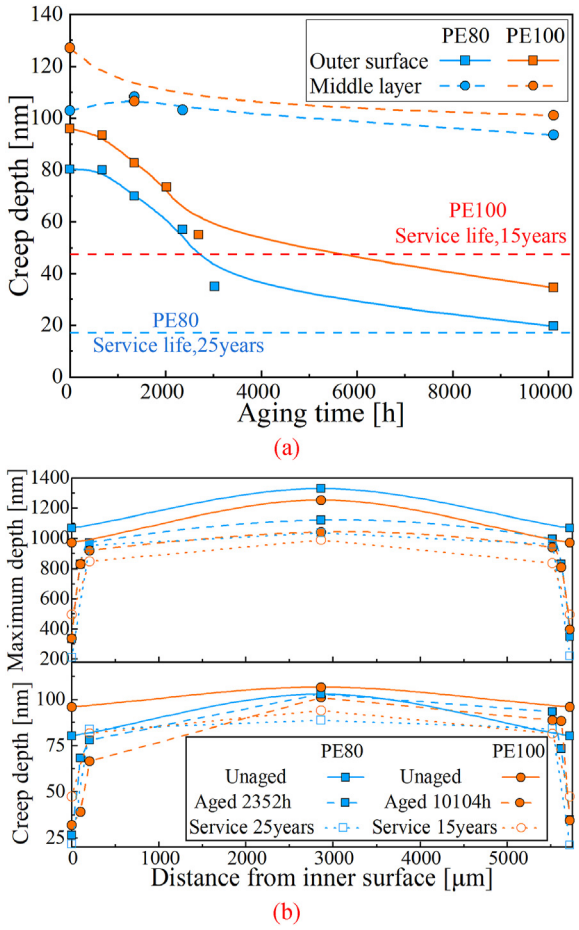


**Fig. 8 – Changes in creep depth with aging time (a) and spatial distribution of the maximum depth and creep depth (b).**

60.0% in outer layer respectively. In addition, the creep depths of the outer layer of PE80 after served 25 years and PE100 after served 15 years are marked in Fig. 8 by dotted lines. As shown in Fig. 8(b), both of the two parameters show obvious non-uniform characteristics, and the value of the middle layer is larger than the surrounding area, nomatter outer layer or inner layer.

Fig. 9(a) and(A) show the typical displacement profiles of PE80 after aging 3024 h and PE100 after aging 2688 h, respectively, during the holding period with a constant load of 1 mN. Creep displacement during holding stage is fitted by using Eq. (15). It is apparent from Fig. 9(a) and (A) that slope of the creep curve become nearly constant (quasi-steady creep, stage II) at the end of holding period which gives the value of creep rate. Creep rate is obtained from the linear curve fitting during quasi-steady stage, as shown in Fig. 9(a) and (A). Fig. 9(b) and (B) show all strain rate profiles of PE80 and PE100 with time during 30 s holding stage at the same peak load. With increasing aging time, the stage II of creep was observed for both materials. It's clear that the quasi-steady stage of the creep has been reached after approximately 20 s for PE80 aged 3024 h, 10104 h and service for 25 years, or for PE100 aged 2688 h, 10104 h and service for 15 years. The creep stress exponent, which identifies the dominated creep mechanism and creep stability is an important parameter for analyzing creep behavior. Stress exponent during steady state creep is obtained by the slope of ln ($d\varepsilon/dt$) versus ln ($\sigma$) within the quasi-steady creep stage, as shown in Fig. 9(c) and (C). The linear fitting in the initial steady state region of the plot gives the value of stress exponent.

A good agreement is observed between the experimental data and the generalized Kelvin model as shown in Tables 1 and 2 Under the accelerated conditions, significant reductions in $h_e$ indicate a reduction of the elasticity for the both materials. What's more, the elastic deformation of the PE80 is smaller than that of the PE100 during most of the exposure times except for 672 h. The time-dependent deformation ($h_1$) which is considered as inelastic response, shows a similar trend to $h_e$ ($h_2$ or $h_3$ exhibit a little change). A reasonable interpretation is that both $h_e$, and $h_i$ are proportional to the stiffness [52], and accelerated aging may cause the material to harden and creep displacement to decrease. Moreover, for all PE pipe samples, $\mu_0$ increases with exposure time. Relative study demonstrates that creep deformation is caused by polymer chain slip, crystal rotation and interlayer separation [53], which can be divided into viscoelasticity and plastic deformation of the material. But it should be noted that the plastic deformation is insignificant during the indentation creep while the load holds at a constant value [47]. In addition, available research indicates that the lower crystallinity can accelerate the creep deformation of PE [54]. Thus, a reduction of creep deformation might clarify a fact that the crystallinity increased with aging time.

The elastic modulus and hardness of the materials were calculated and plotted separately by using two methods (the energy-based method and O– P method) and the corresponding testing data were listed in Fig. 10. Obviously, the almost indistinguishable results of the two methods shown in Fig. 10(a), indicate that the energy-based method to calculate the contact stiffness is not only suitable for cementitious materials [17,39] and rocks [19], but also for PE materials. Then, for the sake of convenience, only the results calculated by using energy-based method would be shown later. In addition, as seen in Fig. 10(b-c), it shows the elastic modulus and hardness of the PE80 and PE100 specimens with different aging time and at various positions, respectively. Apparently, with the increment of aging time, the elastic modulus and hardness of the materials also show obvious characteristics of the time- and space-dependent distribution. As listing in Fig. 10(b), the elastic modulus and hardness of the outer layer of the pipe substantially increase with exposure time, while in the middle layer they show an extremely slow increase. In addition, the PE100 demonstrates a greater elastic modulus and hardness than that of the PE80 at the early aging stage, which reveals it posess greater initial stiffness. However, significant changes occur in these two parameters of the PE80 than those of the PE100 from approximate 2500 h–10104 h, which indicates an approximately lower resistance to the elevated temperatures and pressures. One possible reason is that the stiffness is proportional to the crystallinity [55], and the crystallinity in the original PE100 is higher than that in the PE80, but lower than the latter as the thermo-oxidative aging proceeds. Additionally, the obvious non-uniform aging characteristics can be seen in Fig. 10(c). Due to the adequate

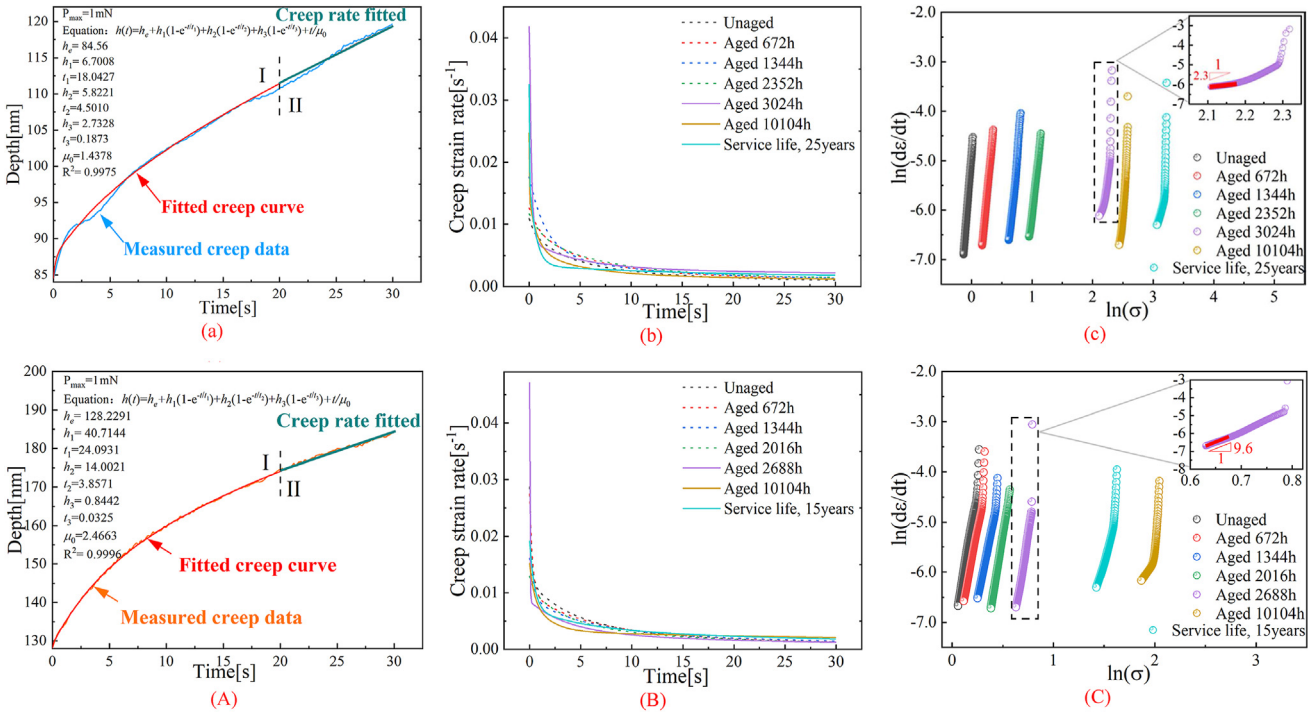


**Fig. 9 – The depth profile of PE80 aged 3024 h (a) and PE100 aged 2688 h (A), and fitted curve using Eq. (15); the strain rate profile of PE80 (b), and PE100 (B); the corresponding ln (dε/dt)-ln (σ) plot of strain rate vs. stress.**

oxygen supply accelerating aging process, it is conceivable that the elastic modulus and hardness of the inner and outer layers of the pipe are greater than those of the middle layer and that is exactly what happened as shown in Fig. 10. Furthermore, it can be seen that under natural age, the PE80 has greater elastic modulus and hardness after 25 years of service operation comparing to accelerated aged 2352 h, while the PE100 has less elastic modulus and hardness after 15 years of service operation when compared to accelerated aged 10104 h. These smaller changes in creep depth, elastic modulus and hardness shown in Figs. 8 and 10, might reveal that PE pipes operate at a slow aging rate in the natural environment.

Changes in relative plastic/elastic behavior of the material are quantified by plasticity index, as shown in Fig. 11 (a) and (b). Under accelerated conditions, stepwise reductions in plasticity index within a relevant small range (i.e., 0.5–0.75) indicate a progressive reduction in the plastic deformation. As a semi-crystalline polymer, the PE structure consists of amorphous region (semi-crystalline region), the crystalline

**Table 1 – The generalized Kelvin model fitting parameters with different aging times for PE80.**

| Aging time | $h_e$ (nm) | $h_1$ (nm) | $t_1$ (s) | $h_2$ (nm) | $t_2$ (s) | $h_3$ (nm) | $t_3$ (s) | $\mu_0$ (s/nm) | $R^2$ |
|---|---|---|---|---|---|---|---|---|---|
| 0 h | 148.35 | 45.52 | 12.57 | 0.69 | 11.45 | 2.88 | 0.36 | 1.27 | 0.9998 |
| 672 h | 136.19 | 44.42 | 12.38 | 1.84 | 11.32 | 3.52 | 0.74 | 1.21 | 0.9999 |
| 1344 h | 140.15 | 35.35 | 12.18 | 1.06 | 11.65 | 1.72 | 0.95 | 1.32 | 0.9979 |
| 2352 h | 115.98 | 24.99 | 10.95 | 1.93 | 11.98 | 5.18 | 1.10 | 1.39 | 0.9998 |
| 3024 h | 84.56 | 6.70 | 5.82 | 2.73 | 18.04 | 4.50 | 0.19 | 1.44 | 0.9975 |
| 10104 h | 81.41 | 6.57 | 5.05 | 1.79 | 20.91 | 4.74 | 0.78 | 3.52 | 0.9874 |
| Service 25 years | 82.41 | 6.79 | 4.43 | 1.84 | 67.91 | 15.01 | 0.60 | 3.45 | 0.9754 |

**Table 2 – The generalized Kelvin model fitting parameters with different aging times for PE100.**

| Aging time | $h_e$ (nm) | $h_1$ (nm) | $t_1$ (s) | $h_2$ (nm) | $t_2$ (s) | $h_3$ (nm) | $t_3$ (s) | $\mu_0$ (s/nm) | $R^2$ |
|---|---|---|---|---|---|---|---|---|---|
| 0 h | 183.71 | 53.91 | 19.46 | 2.81 | 12.13 | 3.72 | 0.193 | 1.18 | 0.9998 |
| 672 h | 115.47 | 51.01 | 18.12 | 4.11 | 14.17 | 4.51 | 0.276 | 1.15 | 0.9998 |
| 1344 h | 144.87 | 49.57 | 15.73 | 2.04 | 16.57 | 4.41 | 0.37 | 1.25 | 0.9994 |
| 2016h | 137.7 | 47.76 | 15.59 | 0.67 | 15.61 | 3.43 | 0.43 | 1.83 | 0.9997 |
| 2688 h | 128.23 | 40.71 | 14.00 | 0.84 | 24.09 | 3.86 | 0.03 | 2.47 | 0.9996 |
| 10104 h | 93.31 | 38.03 | 3.99 | 0.79 | 49.97 | 1.70 | 0.40 | 2.50 | 0.9920 |
| Service 15 years | 110.37 | 39.69 | 8.27 | 2.55 | 31.02 | 5.39 | 0.48 | 2.49 | 0.9983 |

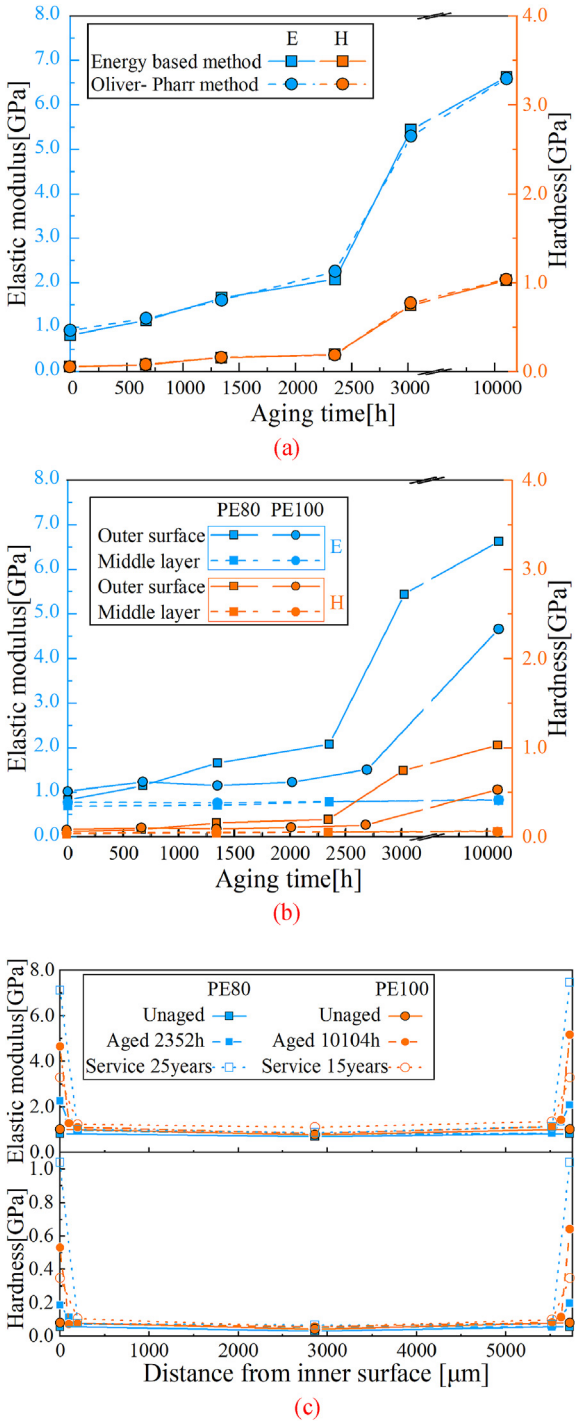


**Fig. 10 – The calculation of elastic modulus and hardness of PE80 outer surface using two methods (a), the two parameters changing with aging time (b) and their distribution along the distance from inner surface (c).**

region and the interzonal region. Many research indicated that thermal oxidation only occur in the amorphous region [2,8]. Once the amorphous regions are oxidized, the fracture of tie-molecular increase, which induces increment of the crystallinity due to cross-linking at an early aging stage. When cross-linking occurred, it would hinder the chain motion and ultimately reduced the ductility of the PE material to some

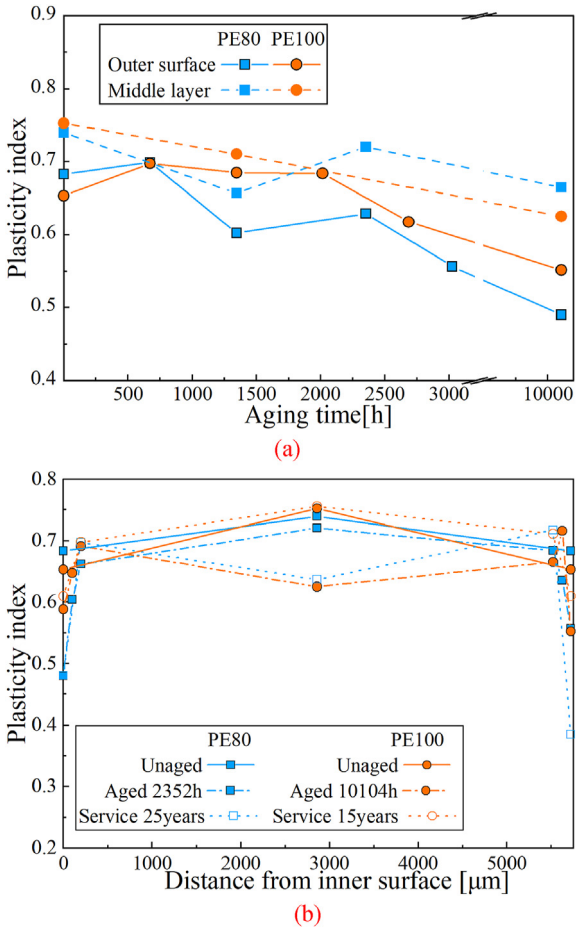


**Fig. 11 – Changes in plasticity index (a) and their distribution along the distance from inner surface (b).**

extent. Macroscopically, the changes in crystalline structure induce the increment or reduction of mechanical properties, where the elastic modulus and hardness increase with the aging time, in contrast creep depth, maximum depth decrease. Similarly, it can be seen from Fig. 11(b) that there is also a significant heterogeneity in the plasticity index among the inner, outer layers and the middle layer.

### 3.2. *DSC and ATR-FTIR results*

Changes in characteristic temperatures of the melting of PE pipes allows to derive some information about the deterioration in the molecular chains during material aging, and thus relevant analysis facilitate understanding of the aging mechanism and process of PE pipes. Fig. 12 presents some DSC results of the inner, middle and outer layer of the PE80 and PE100 samples, respectively. It can be seen that the melting peak temperature (melting point, $T_m$) shows a slow increment with aging time (except for aging 10104 h), and the crystallinity obtained by the total enthalpy method mentioned earlier also shows a stepwise increment, as shown in Fig. 13(a). That is to say, because the more perfect and thicker PE crystals will tend to melt at a higher temperature than smaller crystals, the thickness of the crystals as well as their perfection show a similar trend as $T_m$. When PE pipes suffer from thermo-

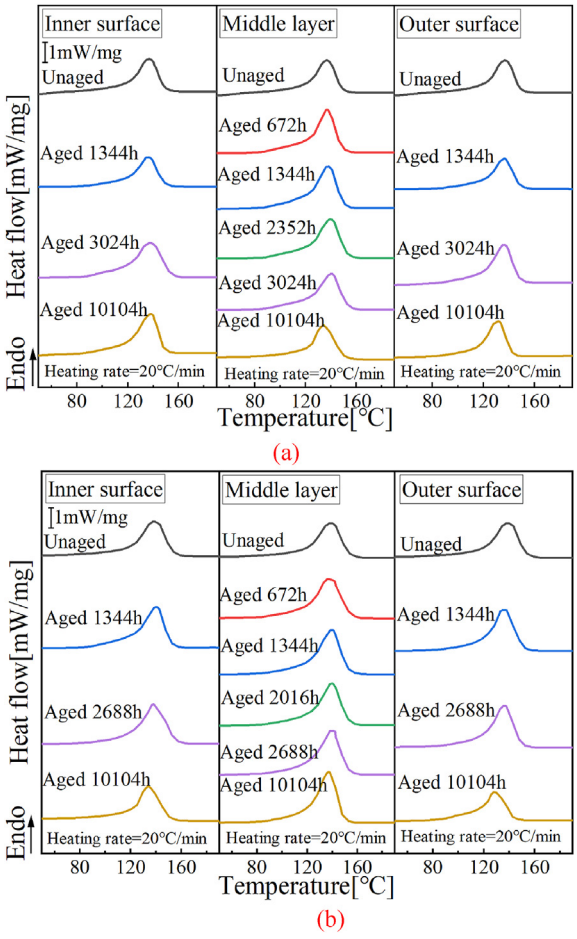


**Fig. 12 – DSC curves of aged PE pipes: (a) PE80 and (b) PE100.**

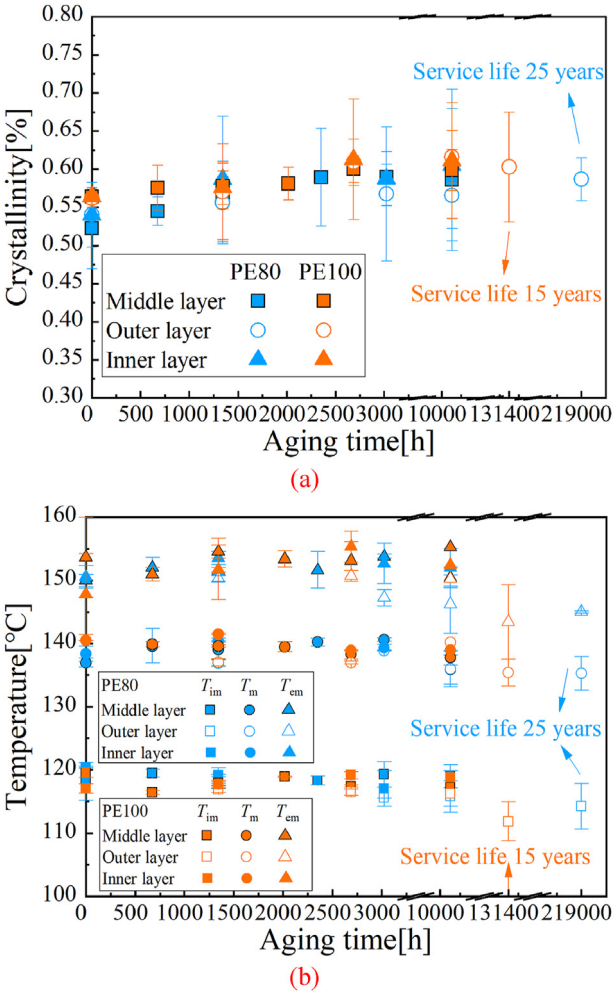


**Fig. 13 – Aging-induced changes in crystallinity (a), initial melting temperature, melting point and end melting temperature for PE pipes (b).**

oxidative aging, the chain scission caused by aging and degradation of the material can lead to chemi-crystallization, which results in the increasing of crystallinity. In addition, as shown in Fig. 13(b), the other characteristic temperatures of the melting including the initial melting temperature (or called onset temperature, $T_{im}$) and end melting temperature ($T_{em}$) were extracted. Significant temporal and spatial dependence was observed for the crystallinity, melting point, initial melting temperature, end melting temperature. With the increment of exposure time, all values of initial melting temperature of the two types of PE pipes have remained on a downward trend (especially in inner or outer layer of samples), where the $T_{im}$ value of the outer layers of the PE80 and PE100 pipe decreases from 120.4 °C to 117.2 °C–114.3 °C and 111.9 °C, respectively, while the $T_{im}$ value of the middle layers of the PE80 or PE100 pipe actually reduces a little. Additionally, the end melting temperatures $T_{em}$ of the inner and outer layers of all pipe materials increases firstly and then decreases. The $T_{im}$ and $T_{em}$ value represent the information related to short and long molecular chains, respectively. When the characteristic temperature decreases, it indicates the number of relevant molecular chains drops. In contrast, an increase of the characteristic temperature indicates an increment for the number of molecular chains. In other words, the decline in the initial melting temperature $T_{im}$ indicates the number of short molecular chains of pipe material descend, while the increase in the end melting temperature $T_{em}$ implies an increment of the long molecular chains.

Additionally, the spectra of the outer surface of the PE pipes with different aging times are shown in Fig. 14. In addition, the aging degree of the two PE materials was quantitatively characterized using the carbonyl index calculation method mentioned earlier, and the results are shown in Fig. 15. As the general characteristics of the infrared spectrum of high density polyethylene, all the infrared spectrum curves obtained have two absorption peaks around 2900 $cm^{-1}$ and one strong absorption peak at 1460 $cm^{-1}$ and 720 $cm^{-1}$ respectively. Based on free radical theory, the majority of the oxidation degradation products are the carbonyl-containing organics with small molecular weights, including ester (1740 $cm^{-1}$), ketone (1715 $cm^{-1}$), aldehyde (1725 $cm^{-1}$) and carboxylic acid (1705 $cm^{-1}$) [56]. As shown in Fig. 14, the wavenumbers near 1740, 1650 $cm^{-1}$ and 1040 $cm^{-1}$ present obvious absorption peaks, which implies the existence of

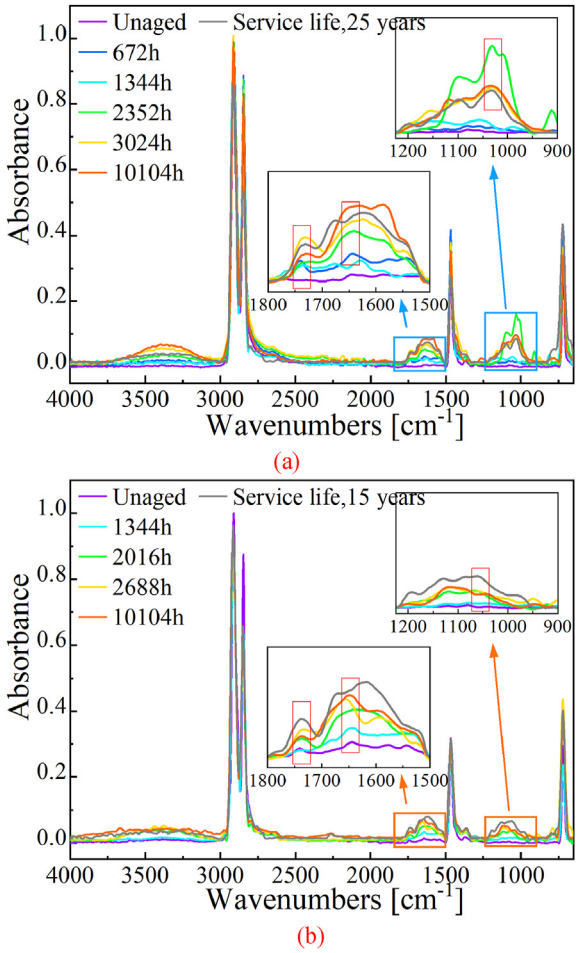


**Fig. 14 – FTIR spectrums of PE80 (a) and PE100 (b) exposed to pressurized air.**

degradation products. Because these peaks present the stretching vibration of the C=O of ester, the C=C bond and the C–O bond of alcohol structure or anhydride [8], respectively. It can be seen from Fig. 15 that the carbonyl index of PE80 and PE100 pipes gradually increase with the aging time.

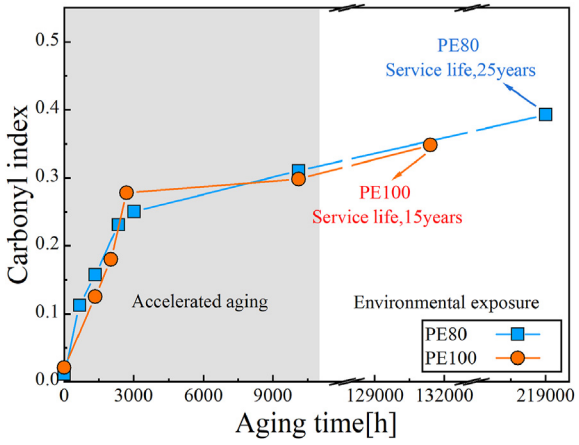


**Fig. 15 – Carbonyl index change as a function of PE grades and aging time (including PE pipes with different service life).**

The similar CI results of PE80 and PE100 pipes confirm that the two pipe materials are comparably deteriorated under high temperature and pressure exposure.

### 3.3. *Correlation between mechanical property and crystalline structure*

Fig. 16 (a) to (c) show the relationship between elastic modulus and hardness, elastic modulus and creep depth, and elastic

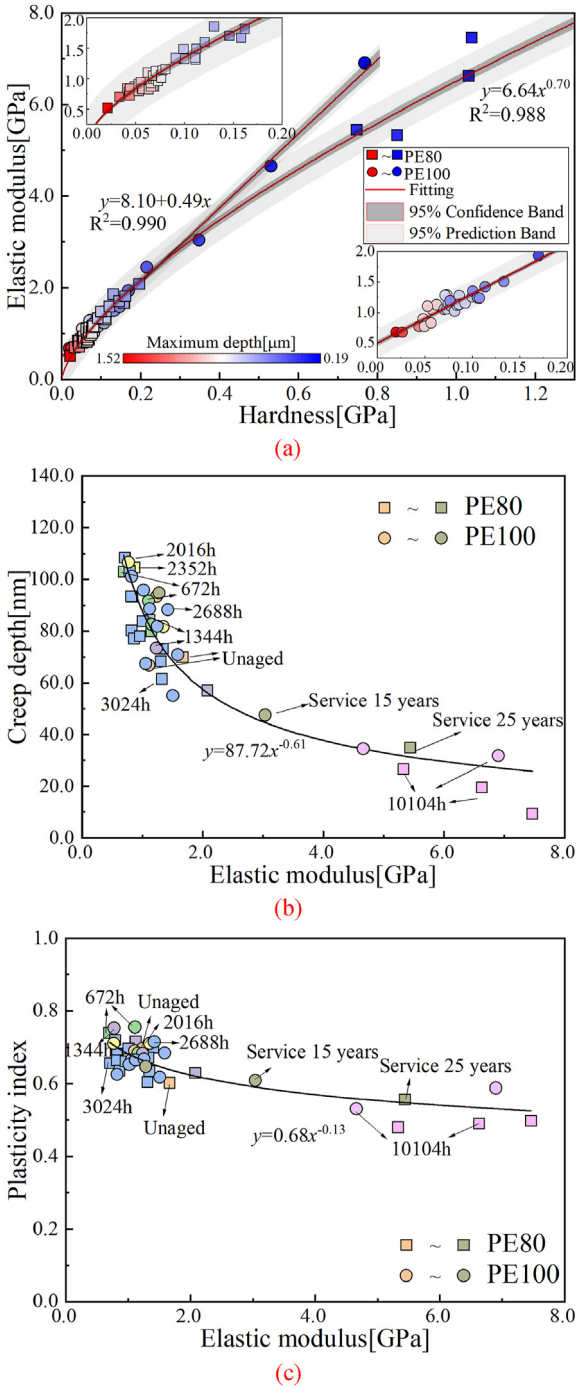


**Fig. 16 – The correlation between (a) hardness and elastic modulus, (b) elastic modulus and creep depth, (c) elastic modulus and plasticity index.**

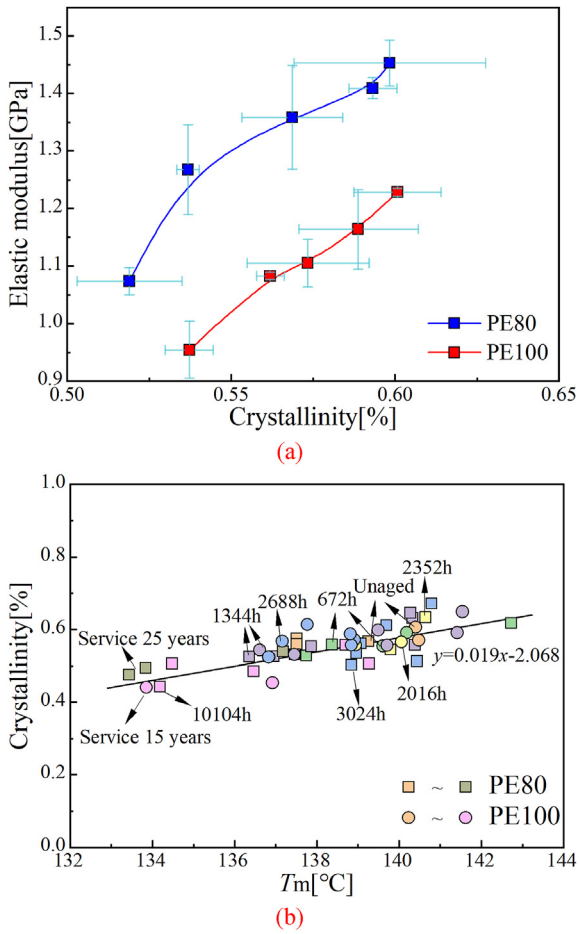


**Fig. 17 – Correlations between elastic modulus and crystallinity (a), and crystallinity as a function of $T_m$ with different aging times (b).**

modulus and plasticity index obtained from nanoindentation tests, respectively. The fitted curves and 95% confidence bands and prediction bands are presented in Fig. 16(a). It can be seen that the elastic modulus and hardness of PE100 show a linear relationship, in which the $R^2$ values equals to 0.99 and is larger than 0.95. In addition, almost all data points fall into the above confidence and prediction bands. However, the elastic modulus and hardness of PE80 show a power function relationship, where the $R^2$ value is also larger than 0.95. In fact, in a small range, the elastic modulus and hardness of PE80 is also close to linearly dependent. It can be understood that an increase in the elastic modulus is proportional to the hardness, where the physical mechanism behind them is the same-an increase in crystallinity results in a denser material. Additionally, as seen in Fig. 16(b) and (c), the creep depth and plasticity index of PE pipes show a power function of the elastic modulus, where the index of the function is less than zero. In other words, the larger the elastic modulus comes, the smaller corresponding creep depth and plasticity index. Moreover, different colors are used in Fig. 16 to indicate different aging times, so that it is more intuitive to see the stepwise reduction of creep depth and plasticity index as aging proceeds with the progressive increase of elastic modulus.

As a semi-crystalline polymer, the mechanical properties, such as elastic modulus, hardness, etc. of PE pipes, are closely related to crystallographic factors such as crystallinity. There are even related reports also indicate that crystallinity also affects the friction and wear properties of the material [57]. Fig. 17 shows the relationship between crystallinity and elastic modulus of PE pipes. Obviously, the mechanical property-elastic modulus shows a roughly proportional to crystallinity. Moreover, for all testing samples, the values of crystallinity were plotted as a function of $T_m$ in Fig. 17(b). Similarly, the crystallinity is proportional to $T_m$, but the data points are discretely distributed around the fitting straight line in Fig. 17(b), indicating that although there is a linear relationship, the linear correlation between crystallinity and $T_m$ is a bit weak. In conclusion, these above results indicate that crystallinity is the main factor affecting the variation of mechanical properties of PE pipes, and a good correlation exists between crystallinity and mechanical properties-elastic modulus.

## 4. Conclusions

In this paper, the mechanical, physical and chemical properties of two types of aged polyethylene pipes are systematically investigated by using nanoindentation, DSC and FTIR. The nanoindentation test can be used to characterize the thermal oxidation of PE pipes, especially to reflect the heterogeneity of aging properties, and can promote the accuracy of mechanical properties characterization and possess well fitness for PE pipes in accelerated aging conditions or in-service. In addition, it also correlates well with other characterization methods. The energy-based method to calculate the contact stiffness is not only suitable for cementitious materials and rocks, but also for PE materials. What's more, the nanoindentation creep tests can not only resolve the difficult and inaccurate to calculate the initial contact stiffness using the slope in O–P method, but also can extract some more detailed parameters that are more representative of the differences in material deformation with aging time. With increasing aging time, the stage II of creep was observed for both materials even with a creep time of only 30s. The generalized Kelvin model had been used to fit the nanoindentation creep data for PE pipes, and the creep curves of the two types of PE materials were further analyzed to extract representative parameters to represent those differences in material deformation. As exposure time progresses, significant temporal and spatial dependence was observed for the mechanical properties-elastic modulus, hardness, plasticity index, creep properties and physic properties-crystallinity, melting point, initial melting temperature, end melting temperature. There is an obvious correlation between physical properties and mechanical properties, the elastic modulus shows a roughly proportional to crystallinity. All results indicate that

crystallinity plays a dominant role on mechanical performances of PE pipes.

## Author statement

**Sixi Zha**: Conceptualization, Methodology, Data curation, Characterization, Formal analysis, Investigation, Methodology, Validation, Software, Writing original draft.

**Hui-qing Lan**: Investigation, Data curation, Methodology, Experiment, Writing - review & editing.

**Nan Lin**, **Yueming Liu** and **Tao Meng**: Investigation, Resources, Experiment, Review & editing.

## Declaration of Competing Interest

The authors declare that they have no known competing financial interests or personal relationships that could have appeared to influence the work reported in this paper.

## Acknowledgment

This work was supported by the National Key Research and Development Program of China (No. 2021YFC2203601) and Youth Foundation of China Special Equipment Inspection and Research Institute (2022 Youth 09).

## REFERENCES

[1] Weon J-I. Effects of thermal ageing on mechanical and thermal behaviors of linear low density polyethylene pipe. Polym Degrad Stabil 2010;95(1):14–20. doi.org/10.1016/j.polymdegradstab.2009.10.016.

[2] Mariaa R, Rodea K, Schuster T. Ageing study of different types of long-term pressure tested PE pipes by IR-microscopy. Polymer 2015;61:131–9. https://doi.org/10.1016/j.polymer.2015.01.062.

[3] Zhang J, Xiao Y, Liang Z. Mechanical behaviors and failure mechanisms of buried polyethylene pipes crossing active strike-slip faults. Compos B Eng 2018;154:449–66. https://doi.org/10.1016/j.compositesb.2018.09.006.

[4] Hassinen J, Lundbäck M, Ifwarson M, Gedde UW. Deterioration of polyethylene pipes exposed to chlorinated water. Polym Degrad Stabil 2004;84(2):261–7. https://doi.org/10.1016/j.polymdegradstab.2003.10.019.

[5] Yu W, Azhdar B, Andersson D, Reitberger T, Hassinen J, Hjertberg T, et al. Deterioration of polyethylene pipes exposed to water containing chlorine dioxide. Polym Degrad Stabil 2011;96(5):790–7. https://doi.org/10.1016/j.polymdegradstab.2011.02.009.

[6] Yu W, Reitberger T, Hjertberg T, Oderkerk J, Costa FR, Gedde UW. Antioxidant consumption in squalane and polyethylene exposed to chlorinated aqueous media. Polym Degrad Stabil 2012;97(11):2370–7. https://doi.org/10.1016/j.polymdegradstab.2012.07.038. Polym. Degrad. Stabil.

[7] Zha S, Lan H-Q, Lin N, Meng T. Degradation and characterization methods for polyethylene gas pipes after natural and accelerated aging. Polym Degrad Stabil 2023:208. https://doi.org/10.1016/j.polymdegradstab.2022.110247.

[8] Gong Y, Wang S-H, Zhang Z-Y, Yang X-L, Yang Z-G, Yang H-G. Degradation of sunlight exposure on the high-density polyethylene (HDPE) pipes for transportation of natural gases. Polym Degrad Stabil 2021;194:109752. https://doi.org/10.1016/j.polymdegradstab.2021.109752.

[9] Pospíšil J, Horák Z, Pilař J, Billingham NC, Zweifel H, Nešpůrek S. Influence of testing conditions on the performance and durability of polymer stabilisers in thermal oxidation. Polym Degrad Stabil 2003;82(2):145–62. https://doi.org/10.1016/S0141-3910(03)00210-6.

[10] Cunliffe AV, Davis A. Photo-oxidation of thick polymer samples- Part II the influence of oxygen diffusion on the natural and artificial weathering of polyolefins. Polym Degrad Stabil 1982;4(1):17–37. https://doi.org/10.1016/0141-3910(82)90003-9.

[11] Gillen KT, Clough RL. Rigorous experimental confirmation of a theoretical model for diffusion-limited oxidation. Polymer 1992;33(20):4358–65. https://doi.org/10.1016/0032-3861(92)90280-A.

[12] Blivet C, Larché J-F, Israëli Y, Bussière P-O, Gardette Jean-Luc. Thermal oxidation of cross-linked PE and EPR used as insulation materials: multi-scale correlation over a wide range of temperatures. Polym Test 2021;93:106913. https://doi.org/10.1016/j.polymertesting.2020. 106913.

[13] Linde E, Nilsson F, Barrett M, Hedenqvist MS, Celina MC. Time- and feedback-dependent DLO phenomena in oxidative polymer aging. Polym Degrad Stabil 2021;189. https://doi.org/10.1016/j.polymdegradstab.2021.109598.

[14] Zha S, Lan H-q, Huang H. Review on lifetime predictions of polyethylene pipes: limitations and trends. Int J Pres Ves Pip 2022;198:104663. https://doi.org/10.1016/j.ijpvp.2022.104663.

[15] Pertin T, Minatchy G, Adoue M, Flory A, Romana L. Investigation of nanoindentation as a fast characterization tool for polymer degradation study. Polym Test 2020;81. https://doi.org/10.1016/j.polymertesting.2019.106194.

[16] Michler GH, Baltá-Calleja FJ. Mechanical properties of polymers based on nanostructure and morphology. Taylor & Francis; 2016.

[17] Jha KK, Suksawang N, Lahiri D, Agarwal A. A novel energy-based method to evaluate indentation modulus and hardness of cementitious materials from nanoindentation load-displacement data. Mater Struct 2014;48(9):2915–27. https://doi.org/10.1617/s11527-014-0367-7.

[18] Bédoui F, Sansoz F, Murthy NS. Incidence of nanoscale heterogeneity on the nanoindentation of a semicrystalline polymer: experiments and modeling. Acta Mater 2008;56(10):2296–306. https://doi.org/10.1016/j.actamat.2008.01.021.

[19] Liu K, Ostadhassan M, Bubach B. Applications of nano-indentation methods to estimate nanoscale mechanical properties of shale reservoir rocks. J Nat Gas Sci Eng 2016;35:1310–9. https://doi.org/10.1016/j.jngse.2016.09.068.

[20] Fulcher JT, Lu YC, Tandon GP, Foster DC. Thermomechanical characterization of shape memory polymers using high temperature nanoindentation. Polym Test 2010;29(5):544–52. https://doi.org/10.1016/j.polymertesting.2010.02.001.

[21] Maxwell AS, Monclus MA, Jennett NM, Dean G. Accelerated testing of creep in polymeric materials using nanoindentation. Polym Test 2011;30(4):366–71. https://doi.org/10.1016/j.polymertesting.2011.02.002.

[22] Moniruzzaman M, Zioupos P, Fernando GF. Investigation of reversible photo-mechanical properties of azobenzene-based polymer films by nanoindentation. Scripta Mater 2006;54(2):257–61. https://doi.org/10.1016/j.scriptamat.2005.09.025.
[23] Flores A, Ania F, Baltá-Calleja FJ. From the glassy state to ordered polymer structures: a microhardness study. Polymer 2009;50(3):729–46. https://doi.org/10.1016/j.polymer.2008.11.037.
[24] Milhans J, Li DS, Khaleel M, Sun X, Al-Haik MS, Harris A, et al. Mechanical properties of solid oxide fuel cell glass-ceramic seal at high temperatures. J Power Sources 2011;196(13):5599–603. https://doi.org/10.1016/j.jpowsour.2011.02.033.
[25] Christöfl P, Czibula C, Seidlhofer T, Berer M, Macher A, Helfer E, et al. Morphological characterization of semi-crystalline POM using nanoindentation. Int J Polym Anal Char 2021;26(8):692–706. https://doi.org/10.1080/1023666x.2021. 1968122.
[26] Kumar A, Nayak SK, Banerjee A, Laha T. Multi-scale indentation creep behavior in Fe-based amorphous/nanocrystalline coating at room temperature. Mater Lett 2021;283. https://doi.org/10.1016/j.matlet.2020.128768.
[27] Wang C, Liao Y-C, Chu JP, Hsueh C-H. Viscous flow and viscosity measurement of low-temperature imprintable AuCuSi thin film metallic glasses investigated by nanoindentation creep. Mater Des 2017;123:112–9. https://doi.org/10.1016/j.matdes.2017.03.043.
[28] Li H, Chen J, Chen Q, Liu M. Determining the constitutive behavior of nonlinear visco-elastic-plastic PMMA thin films using nanoindentation and finite element simulation. Mater Des 2021:197. https://doi.org/10.1016/j.matdes.2020.109239.
[29] Han G, Marimuthu KP, Lee H. Evaluation of thin film material properties using a deep nanoindentation and ANN. Mater Des 2022;221. https://doi.org/10.1016/j.matdes.2022. 111000.
[30] Zhao Y, Li H, Zhang Z, Celli J, Percec S, Ren F. Nanoindentation study of time-dependent mechanical properties of ultra-high-molecular-weight polyethylene (UHMWPE) at different temperatures. Polym Test 2020;91. https://doi.org/10.1016/j.polymertesting.2020.106787.
[31] Dong P, Zhang Q, Wang K, Zhu B-H, Su W, Li J-F, et al. Pursuit of the correlation between yield strength and crystallinity in sintering-molded UHMWPE. Polymer 2021;215. https://doi.org/10.1016/j.polymer.2020.123352.
[32] Walter C, Antretter T, Daniel R, Mitterer C. Finite element simulation of the effect of surface roughness on nanoindentation of thin films with spherical indenters. Surf Coating Technol 2007;202(4–7):1103–7. https://doi.org/10.1016/j.surfcoat.2007.07.038.
[33] An L, Zhang D, Zhang L, Feng G. Effect of nanoparticle size on the mechanical properties of nanoparticle assemblies. Nanoscale 2019;11(19):9563–73. https://doi.org/10.1039/C9NR01082C.
[34] Poduška J, Kučera J, Hutař P, Ševčík M, Křivánek J, Sadílek J, et al. Residual stress distribution in extruded polypropylene pipes. Polym Test 2014;40:88–98. https://doi.org/10.1016/j.polymer-testing.2014.08.006.
[35] Oliver WC, Pharr GM. An improved technique for determining hardness and elastic modulus using load and displacement sensing indentation experiments. J Mater Res 1992;7(6):1564–83. https://doi.org/10.1557/JMR.1992.1564.
[36] Laurent-Brocq M, Bejanin E, Champion Y. Influence of roughness and tilt on nanoindentation measurements: a quantitative model. Scanning 2015;37(5):350–60. https://doi.org/10.1002/sca. 21220.
[37] Li X, Zhang W, Han M, Xie F, Li D, Zhang J, et al. Indentation size effect: an improved mechanistic model incorporating surface undulation and indenter tip irregularity. J Mater Res Technol 2023;23:143–53. https://doi.org/10.1016/j.jmrt.2023.01.001.
[38] Ebenstein DM, Pruitt LA. Nanoindentation of biological materials. Nano Today 2006;1(3):26–33. https://doi.org/10.1016/s1748-0132(06)70077-9.
[39] Jha K, Suksawang N, Lahiri D, Agarwal A. Energy-based analysis of nanoindentation curves for cementitious materials. ACI Mater J 2012;109. https://doi.org/10.1061/(ASCE)ST.1943-541X.0000413.
[40] Sreeram A, Patel NG, Venkatanarayanan RI, McLaughlin JB, DeLuca SJ, Yuya PA, et al. Nanomechanical properties of poly(para-phenylene vinylene) determined using quasi-static and dynamic nanoindentation. Polym Test 2014;37:86–93. https://doi.org/10.1016/j.polymertesting.2014.04.012.
[41] Briscoe BJ, Pelillo E, Fiori L. Nano-indentation of polymeric surfaces.pdf. J Phys D Appl Phys 1998;31(19):2395–405. https://doi.org/10.1088/00223727/31/19/006.
[42] Gao J, Xu Z, Fang X, He J, Li W, Du X, et al. Enhancing creep resistance of aged Fe–Cr–Ni medium-entropy alloy via nano-sized Cu-rich and NbC precipitates investigated by nanoindentation. J Mater Res Technol 2022;20:1860–72. https://doi.org/10.1016/j. jmrt.2022.08.018.
[43] Xing X, Wang Y, Xiao G, Yu S, Ma Y, Shu X, et al. Rate-dependent indentation size effect on hardness and creep behavior of a titanium metallization film on alumina substrate. J Mater Res Technol 2021;15:4662–71. https://doi.org/10.1016/j.jmrt.2021. 10.101.
[44] Wang J, Yang C, Liu Y, Li Y, Xiong Y. Using nanoindentation to characterize the mechanical and creep properties of shale: load and loading strain rate effects. ACS Omega 2022;7(16):14317–31. https://doi.org/10.1021/acsomega.2c01190.
[45] Li H, Ngan AHW. Size effects of nanoindentation creep. J Mater Res 2004;19(2):513–22. https://doi.org/10.1557/jmr.2004.19.2.513.
[46] Fan Q, Gan K, Yan D, Li Z. Nanoindentation creep behavior of diverse microstructures in a pre-strained interstitial high-entropy alloy by high-throughput mapping. Mater Sci Eng 2022;856. https://doi.org/10.1016/j.msea.2022.143988.
[47] Yang S, Zhang Y-W, Zeng K. Analysis of nanoindentation creep for polymeric materials. J Appl Phys 2004;95(7):3655–66. https://doi.org/10.1063/1.1651341.
[48] Oral E, Malhi AS, Muratoglu OK. Mechanisms of decrease in fatigue crack propagation resistance in irradiated and melted UHMWPE. Biomaterials 2006;27(6):917–25. https://doi.org/10.1016/j.biomaterials.2005.06.025.
[49] Almond J, Sugumaar P, Wenzel MN, Hill G, Wallis C. Determination of the carbonyl index of polyethylene and polypropylene using specified area under band methodology with ATR-FTIR spectroscopy. E-Polymers 2020;20(1):369–81. https://doi.org/10.1515/epoly-2020-0041.
[50] Sun N, Wenzel M, Adams A. Morphology of high-density polyethylene pipes stored under hydrostatic pressure at elevated temperature. Polymer 2014;55(16):3792–800. https://doi.org/10.1016/j.polymer.2014.05.056.
[51] Lu Y, Yang W, Zhang K, Yang M-b. Stress relaxation behavior of high density polyethylene (HDPE) articles molded by gas-assisted injection molding. Polym Test 2010;29(7):866–71. https://doi.org/10.1016/j.polymertesting.2010.03.005.

[52] Li H, Xi J, Zhao Y, Ren F. Mechanical properties of polydopamine (PDA) thin films. RSC Adv 2019;4(7):405–12. https://doi.org/10.1557/adv.2019.52.
[53] Hamouda HBH, Simoes-betbeder M, Grillon F, Blouet P, Billon N, Piques R. Creep damage mechanisms in polyethylene gas pipes. Polymer 2001;42(12):5425–37. https://doi.org/10.1016/S0032-3861(00)00490-0.
[54] Nitta K-h, Maeda H. Creep behavior of high density polyethylene under a constant true stress. Polym Test 2010;29(1):60–5. https://doi.org/10.1016/j.polymertesting.2009.09.005.
[55] Lim CT, Tan EPS, Ng SY. Effects of crystalline morphology on the tensile properties of electrospun polymer nanofibers. Appl Phys Lett 2008;92(14). https://doi.org/10.1063/1.2857478.
[56] Gedde UW, Ifwarson M. Molecular structure and morphology of crosslinked polyethylene in an aged hot-water pipe. Polym Eng Sci 1990;30(4):202–10. https://doi.org/10.1002/pen.760300403.
[57] Kanaga Karuppiah KS, Bruck AL, Sundararajan S, Wang J, Lin Z, Xu ZH, et al. Friction and wear behavior of ultra-high molecular weight polyethylene as a function of polymer crystallinity. Acta Biomater 2008;4(5):1401–10. https://doi.org/10.1016/j.actbio.2008.02.022.